







Controlling the ac Stark effect of RbCs with dc electric and magnetic fieldsJacob A. Blackmore ^{1,*} Rahul Sawant ^{1,†} Philip D. Gregory ¹ Sarah L. Bromley ¹ Jesús Aldegunde,²
Jeremy M. Hutson ^{3,‡} and Simon L. Cornish ^{1,§}¹*Joint Quantum Centre (JQC) Durham-Newcastle, Department of Physics, Durham University, South Road, Durham DH1 3LE, United Kingdom*²*Departamento de Química Física, Universidad de Salamanca, 37008 Salamanca, Spain*³*Joint Quantum Centre (JQC) Durham-Newcastle, Department of Chemistry, Durham University, South Road, Durham DH1 3LE, United Kingdom*

(Received 3 July 2020; accepted 15 September 2020; published 17 November 2020)

We investigate the effects of static electric and magnetic fields on the differential ac Stark shifts for microwave transitions in ultracold bosonic $^{87}\text{Rb}^{133}\text{Cs}$ molecules, for light of wavelength $\lambda = 1064$ nm. Near this wavelength we observe unexpected two-photon transitions that may cause trap loss. We measure the ac Stark effect in external magnetic and electric fields, using microwave spectroscopy of the first rotational transition. We quantify the isotropic and anisotropic parts of the molecular polarizability at this wavelength. We demonstrate that a modest electric field can decouple the nuclear spins from the rotational angular momentum, greatly simplifying the ac Stark effect. We use this simplification to control the ac Stark shift using the polarization angle of the trapping laser.

DOI: [10.1103/PhysRevA.102.053316](https://doi.org/10.1103/PhysRevA.102.053316)**I. INTRODUCTION**

Experimental interest in ultracold molecules is growing rapidly, spurred on by applications spanning precision measurement [1–11], state-resolved chemistry [12–17], dipolar quantum matter [18–22], quantum simulation [23–28], and quantum-information processing [29–35]. Two prominent methods have emerged for producing molecular gases in the ultracold regime. The first relies on association of precooled atoms using magnetoassociation on a Feshbach resonance followed by coherent optical transfer to the rovibronic ground state. When the initial atomic gases are at or near quantum degeneracy, a molecular gas with high phase-space density is produced. Numerous alkali molecules have been created in this way, including KRb [36], Cs₂ [37], Rb₂ [38], RbCs [39,40], NaK [41–43], NaRb [44], and NaLi [45]. Significant progress is also being made toward producing molecules from mixtures of open-shell and closed-shell atoms [46–51]. The second method employs direct laser cooling of molecules. Although molecules have complex level structures that make them difficult to cool, there are a few that have almost closed electronic transitions suitable for laser cooling. So far, laser cooling has been demonstrated for SrF [52–55], YO [56], CaF [57–59], YbF [60], and SrOH [61], with several other species being pursued [62–65].

There are many proposals that use polar molecules confined in optical lattices for the simulation of novel problems in many-body physics [23–28,66–69]. These proposals exploit long-range dipole-dipole interactions between molecules, which can be controlled using dc electric or microwave fields. If the molecules are permitted to tunnel between lattice sites, novel quantum phases, including supersolids and spin glasses, are predicted to emerge [25,26,28,66–69]. Alternatively, if the molecules are pinned to the lattice sites, pseudospin excitations encoded in the rotational states of the molecule can propagate in the lattice due to dipolar spin-exchange interactions. This allows exploration of Hamiltonians relevant to quantum magnetism [23,24,27,70–73]. The rich rotational and hyperfine structure of molecules expands the range of Hamiltonians that are accessible. In both cases, the majority of proposals require high occupancy in the lattice. For atoms, high occupancy may be achieved via the Mott-insulator transition [74]. Extending this to two atomic species and then forming molecules from the atomic pairs can lead to high occupancy for the molecules, as demonstrated for ground-state KRb [75] and RbCs Feshbach molecules [76].

To realize a useful simulator, we need to confine molecules in a lattice or optical tweezers in a way that fulfills several criteria. First, the molecules must be adequately confined. This requires a peak laser intensity of at least a few kW cm⁻². Second, the one-body lifetime, limited by evaporation and off-resonant light scattering, must be much greater than the timescales associated with the evolution of the Hamiltonian under investigation. Third, the ac Stark effect must be controlled such that the coherence time is longer than the characteristic intersite interaction time. Alkali molecules typically have permanent electric dipole moments of ~ 1 D, which for a lattice spacing of ~ 500 nm leads to a dipole-dipole

*j.a.blackmore@durham.ac.uk

†Present address: Midlands Ultracold Atom Research Centre, School of Physics and Astronomy, Birmingham University, Edgbaston Park Road, Birmingham B15 2TT, UK.

‡j.m.hutson@durham.ac.uk

§s.l.cornish@durham.ac.uk

interaction energy $\sim h \times 1$ kHz. Rotational coherence times greater than 10 ms are therefore needed. Finally, for molecules like RbCs, which are transferred to the rovibronic ground state from a Feshbach state, it is desirable that the Feshbach state and the ground state have very similar polarizabilities. This prevents excitation into higher bands of the lattice during the optical transfer to the ground state [38,77]. In the case of RbCs molecules, it has been predicted [78] that this last condition should be satisfied for a lattice wavelength near 1064 nm, motivating the present work.

In this paper, we investigate the ac Stark effect for $^{87}\text{Rb}^{133}\text{Cs}$ molecules (hereafter referred to simply as RbCs) in light of wavelength $\lambda = 1064$ nm. We show that application of a dc electric field parallel to the magnetic field can dramatically simplify the microwave spectrum, as predicted theoretically [79–81]. We demonstrate that this simplification extends to the ac Stark effect. With a careful choice of laser polarization, RbCs in an optical lattice will be suitable for quantum simulation using the $N = 0$ and 1 rotational states. En route, we measure the lifetime of RbCs in the optical trap at $\lambda = 1064$ nm, revealing several unanticipated two-photon resonances, and we accurately determine the isotropic and anisotropic polarizabilities at this wavelength.

The paper is structured as follows. In Sec. II, we present the theory describing the energy-level structure of RbCs in magnetic, electric, and optical fields. We demonstrate how the use of an electric field simplifies the ac Stark effect and permits the creation of magic-angle traps. In Sec. III, we briefly present our experimental setup. In Sec. IV, we investigate the lifetime of RbCs molecules in the 1064 nm trap. In Sec. V, we report measurements of the isotropic and anisotropic polarizabilities at this wavelength. In Sec. VI, we use these results to control the ac Stark effect, with a view to achieving long rotational coherence times for trapped molecules. Finally, in Sec. VII we conclude and consider the implications of our results for quantum science with RbCs molecules.

II. THEORY

We choose to focus on the rotational transition $N = 0 \rightarrow 1$ and we aim to minimize differential ac Stark shifts of this transition for suitable trap depths. To achieve this, we need a detailed understanding of the internal structure of the molecule in the presence of magnetic, electric, and optical fields. In this section, we describe a general Hamiltonian appropriate for diatomic molecules in the lowest vibrational state of a $^1\Sigma$ electronic state, and then we apply it to the specific case of RbCs under experimentally relevant conditions.

A. The molecular Hamiltonian

The effective Hamiltonian for a diatomic molecule in a single vibrational level v of a $^1\Sigma$ electronic state is [79,82]

$$H = H_{\text{rot}} + H_{\text{hf}} + H_{\text{ext}}, \quad (1)$$

where H_{rot} is the Hamiltonian associated with the rotational degree of freedom, H_{hf} represents the hyperfine structure, and H_{ext} is associated with interaction between the molecule and external fields. We will discuss each of these terms below.

The rotational structure for low-lying rotational states is well described by [79,82,83]

$$H_{\text{rot}} = B_v N^2 - D_v N^2 N^2. \quad (2)$$

Here N is the rotational angular momentum operator, B_v is the rotational constant, and D_v is the centrifugal distortion constant. The eigenstates of this Hamiltonian are simply the spherical harmonics; we denote these states by kets $|N, M_N\rangle$, where N is the rotational quantum number and M_N is the projection of the rotational angular momentum onto the space-fixed z axis.

The hyperfine term in (1) has four contributions [79,84],

$$H_{\text{hf}} = H_{\text{quad}} + H_{II}^{(0)} + H_{II}^{(2)} + H_{NI}, \quad (3)$$

where

$$H_{\text{quad}} = \sum_{j=\text{Rb,Cs}} e\mathbf{Q}_j \cdot \mathbf{q}_j, \quad (4a)$$

$$H_{II}^{(0)} = c_4 \mathbf{I}_{\text{Rb}} \cdot \mathbf{I}_{\text{Cs}}, \quad (4b)$$

$$H_{II}^{(2)} = -c_3 \sqrt{6} \mathbf{T}^2(C) \cdot \mathbf{T}^2(\mathbf{I}_{\text{Cs}}, \mathbf{I}_{\text{Rb}}), \quad (4c)$$

$$H_{NI} = \sum_{j=\text{Rb,Cs}} c_j N \cdot \mathbf{I}_j. \quad (4d)$$

H_{quad} represents the interaction between the nuclear electric quadrupole of nucleus j ($e\mathbf{Q}_j$) with the electric field gradient at the nucleus (\mathbf{q}_j). $H_{II}^{(0)}$ and $H_{II}^{(2)}$ are the scalar and tensor nuclear spin-spin interactions, with strengths governed by the coefficients c_4 and c_3 . The second-rank tensors \mathbf{T}^2 describe the angular dependence and anisotropy of the interactions [84]. H_{NI} is the interaction between the nuclear magnetic moments and the magnetic field generated by the rotating molecule, and it has a coupling constant c_j for each of the two nuclei.

The term H_{ext} describes interactions between the molecule and external fields. Here this includes the Zeeman effect, the dc Stark effect, and the ac Stark effect,

$$H_{\text{ext}} = H_{\text{Zeeman}} + H_{\text{dc}} + H_{\text{ac}}. \quad (5)$$

The Zeeman term describes the interaction of the rotational and nuclear magnetic moments with the external magnetic field (\mathbf{B}) and is

$$H_{\text{Zeeman}} = -g_r \mu_N N \cdot \mathbf{B} - \sum_{j=\text{Rb,Cs}} g_j (1 - \sigma_j) \mu_N \mathbf{I}_j \cdot \mathbf{B}. \quad (6)$$

The first term accounts for the magnetic moment generated by the rotation of the molecule, characterized by the rotational g -factor g_r . The second term accounts for the nuclear spin contributions, characterized by the nuclear g -factors g_j shielded isotropically by the factor σ_j [79]. In both terms, μ_N is the nuclear magneton. For our analysis, we designate the axis of the magnetic field \mathbf{B} as the space-fixed z axis and its magnitude as B_z .

The dc Stark term describes the interaction between the molecular dipole moment and a static electric field \mathbf{E} , and is

$$H_{\text{dc}} = -\boldsymbol{\mu} \cdot \mathbf{E}. \quad (7)$$

The matrix elements of the dipole moment operator, $\boldsymbol{\mu}$, are [82]

$$\begin{aligned} & \langle N, M_N | \boldsymbol{\mu} | N', M'_N \rangle \\ &= \sum_{j=-1,0,+1} \mu_v \hat{j} \sqrt{(2N+1)(2N'+1)} (-1)^{M_N} \\ & \times \begin{pmatrix} N & 1 & N' \\ -M_N & j & M'_N \end{pmatrix} \begin{pmatrix} N & 1 & N' \\ 0 & 0 & 0 \end{pmatrix}, \end{aligned} \quad (8)$$

where \hat{j} is a unit vector along the axes $x - iy$, z , and $x + iy$ for $j = -1, 0$, and $+1$, respectively. μ_v is the permanent dipole moment of the molecule in the molecule-fixed frame, and the symbols in parentheses are Wigner $3j$ symbols. $j = -1, 0$, and 1 correspond to σ_+ , π , σ_- transitions, respectively, which can change M_N by $+1, 0$, and -1 when a photon is absorbed. We restrict \mathbf{E} to lie along z , with magnitude E_z , so that only the term with $j = 0$ contributes to the dc Stark effect.

The ac Stark effect arises from the interaction of an off-resonant oscillating electric field \mathbf{E}_{ac} with the frequency-dependent molecular polarizability tensor $\boldsymbol{\alpha}$ [85]. It is

$$H_{ac} = -\frac{1}{2} \mathbf{E}_{ac} \cdot \boldsymbol{\alpha} \cdot \mathbf{E}_{ac}. \quad (9)$$

For a linear diatomic molecule, the polarizability along the internuclear axis, α_{\parallel} , is different from that perpendicular to it, α_{\perp} . The overall polarizability of the molecule is therefore anisotropic. For a molecule oriented at an angle θ to the laser polarization, the polarizability is

$$\begin{aligned} \alpha(\theta) &= \alpha_{\parallel} \cos^2 \theta + \alpha_{\perp} \sin^2 \theta \\ &= \alpha^{(0)} + \alpha^{(2)} P_2(\cos \theta), \end{aligned} \quad (10)$$

where $\alpha^{(0)} = \frac{1}{3}(\alpha_{\parallel} + 2\alpha_{\perp})$, $\alpha^{(2)} = \frac{2}{3}(\alpha_{\parallel} - \alpha_{\perp})$, and $P_2(x) = (3x^2 - 1)/2$ is the second-order Legendre polynomial [85]. We consider the case in which the laser is polarized in the xz plane at an angle β to the z axis. To transform the polarizability from the molecular frame to laboratory coordinates requires a rotation through angle β about y . The matrix elements of (9) in the basis set $|N, M_N\rangle$ are [85]

$$\begin{aligned} & \langle N, M_N | H_{ac} | N', M'_N \rangle \\ &= -\frac{I\alpha^{(0)}}{2\epsilon_0 c} \delta_{N,N'} \delta_{M_N,M'_N} \\ & -\frac{I\alpha^{(2)}}{2\epsilon_0 c} \sum_M d_{M0}^2(\beta) (-1)^{M'_N} \sqrt{(2N+1)(2N'+1)} \\ & \times \begin{pmatrix} N' & 2 & N \\ 0 & 0 & 0 \end{pmatrix} \begin{pmatrix} N' & 2 & N \\ -M'_N & M & M_N \end{pmatrix}. \end{aligned} \quad (11)$$

Here I is the laser intensity, $\delta_{A,B}$ is a Kronecker delta, and $d_{M0}^2(\beta)$ is a reduced Wigner rotation matrix.

The term proportional to the isotropic part, $\alpha^{(0)}$, produces an equal energy shift of all (N, M_N) . The term proportional to the anisotropic part, $\alpha^{(2)}$, has more complicated behavior: for $N > 0$ it has elements both diagonal and off-diagonal in M_N that depend on β . If we consider only matrix elements with $N = N' = 1$, the matrix representation of the term

proportional to $I\alpha^{(2)}$ is

$$\begin{aligned} & \left(\frac{I\alpha^{(2)}}{5 \times 2\epsilon_0 c} \right) \\ & \times \begin{pmatrix} P_2(\cos \beta) & \frac{3}{\sqrt{2}} \sin \beta \cos \beta & -\frac{3}{2} \sin^2 \beta \\ \frac{3}{\sqrt{2}} \sin \beta \cos \beta & -2P_2(\cos \beta) & -\frac{3}{\sqrt{2}} \sin \beta \cos \beta \\ -\frac{3}{2} \sin^2 \beta & -\frac{3}{\sqrt{2}} \sin \beta \cos \beta & P_2(\cos \beta) \end{pmatrix}, \end{aligned} \quad (12)$$

where rows and columns are in the order $M_N, M'_N = -1, 0, 1$.

We construct the Hamiltonian in a fully uncoupled basis set. The eigenstates are

$$|\psi_{\text{hf}}\rangle = \sum_{N,X} A_X |N, M_N\rangle |i_{\text{Rb}}, m_{\text{Rb}}\rangle |i_{\text{Cs}}, m_{\text{Cs}}\rangle, \quad (13)$$

where $|i_j, m_j\rangle$ represents a basis function for nucleus j with nuclear spin i_j and projection m_j , and X collectively represents the quantum numbers M_N, m_{Rb} , and m_{Cs} . At the fields we consider here, it is sufficient to include basis functions with $N \leq 5$. The mixing of different values of N is relatively weak; N is not a good quantum number, but it remains a useful label for the eigenstates.

The hyperfine term in the Hamiltonian mixes states with different values of M_N, m_{Rb} , and m_{Cs} , though it conserves their sum, $M_F = M_N + m_{\text{Rb}} + m_{\text{Cs}}$. It is also weakly off-diagonal in N . Accordingly, the eigenstates can be mixtures of many different rigid-rotor and nuclear-spin states, even in the absence of external fields.

The Zeeman, dc Stark, and ac Stark terms are diagonal in m_{Rb} and m_{Cs} . The Zeeman term is also diagonal in N and M_N . For an electric field along z , the dc Stark term is diagonal in M_N but is off-diagonal in N with $\Delta N = \pm 1$. When $\beta = 0$, so that the trapping laser is polarized along z , H_{ac} is diagonal in M_N but weakly off-diagonal in N with $\Delta N = 0, \pm 2$. Under these circumstances, the entire Hamiltonian is diagonal in M_F , so it is a good quantum number. For $\beta \neq 0$, however, H_{ac} is off-diagonal in M_N and hence in M_F . In this case, no good quantum numbers exist.

B. Application to RbCs

We now apply the full Hamiltonian of (1)–(11) to RbCs molecules in the $v = 0$ state of the $^1\Sigma^+$ electronic state, as used in our experiments. We use the spectroscopic constants tabulated in Ref. [86], determined from microwave spectroscopy or from the calculations of Ref. [79] where necessary. The nuclear spins of ^{87}Rb and ^{133}Cs are $i_{\text{Rb}} = 3/2$ and $i_{\text{Cs}} = 7/2$, respectively. At small magnetic fields ($B_z < 10$ G) these couple to one another and to the rotational angular momentum to form a resultant F . For $N = 0$ there are four zero-field levels with $F = 2, 3, 4$, and 5 ; these split into a total of $(2N+1)(2i_{\text{Rb}}+1)(2i_{\text{Cs}}+1) = 32$ Zeeman sublevels in a magnetic field. For $N = 1$, the number of sublevels is increased to 96 because of the additional rotational angular momentum. We designate individual sublevels $(N, M_F)_k$, where k distinguishes between those with the same values of N and M_F , in order of increasing energy at 181.5 G; the lowest sublevel for each (N, M_F) is designated $k = 0$. The full state

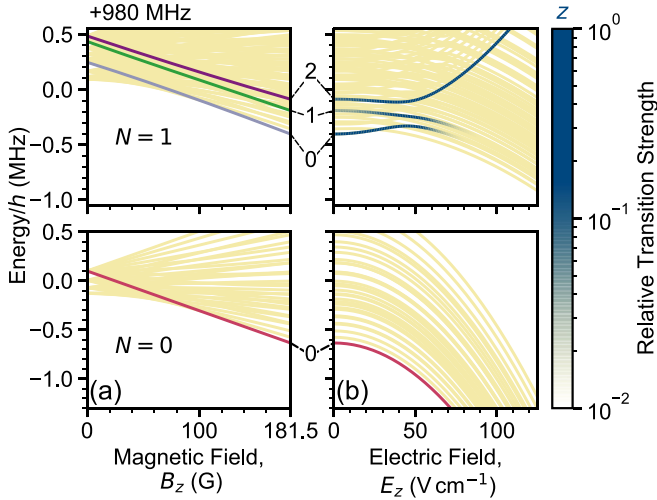


FIG. 1. The hyperfine structure of RbCs. (a) Energy as a function of dc magnetic field. For $N = 0$, the state $(N, M_F)_k = (0, 5)_0$ is highlighted in red and labeled as state 0. For $N = 1$, the states $(1, 5)_k$ are highlighted and labeled with $k = 0, 1, 2$. (b) Energy as a function of dc electric field with magnetic field fixed at $B_z = 181.5$ G. The relative transition strength for transitions from $(0, 5)_0$ for microwaves polarized along z is shown by the blue color map.

compositions, in the uncoupled $|N, M_N, m_{\text{Rb}}, m_{\text{Cs}}\rangle$ basis, of the states discussed in this section are given in the Appendix.

In Fig. 1(a) we show the energies of the sublevels for $N = 0$ and 1 as a function of magnetic field in the absence of dc and ac electric fields. In our apparatus, we produce RbCs molecules at a magnetic field of 181.5 G in the lowest hyperfine sublevel, $(N, M_F)_k = (0, 5)_0$, which has well-defined nuclear spin projections $m_{\text{Rb}} = 3/2$ and $m_{\text{Cs}} = 7/2$. At this magnetic field, F is no longer a good quantum number, but transitions with $\Delta N = 1$ and $\Delta M_F = 0, \pm 1$ have significant strength. In Fig. 1(a), we have highlighted the three sublevels of $N = 1$ with $M_F = 5$. Because of the nuclear quadrupole interaction, Eq. (4a), these states have components with different nuclear spin projections as shown in the Appendix, Table I; this can be exploited to change the nuclear spin state in the ground rotational state [14,80,86–88].

In Fig. 1(b) we show the level energies at 181.5 G as a function of a small electric field $E_z < 150$ V cm $^{-1}$, parallel to the magnetic field. For $N = 0$ the sublevels are parallel to one another as a function of electric field, because every sublevel has the same rotational projection $M_N = 0$. For $N = 1$, by contrast, there is a pattern of crossings and avoided crossings as the states split according to $|M_N|$. The branch with $M_N = 0$ is higher in energy than that with $M_N = \pm 1$, as is shown in Fig. 2(a). The strength of the blue highlighting in Fig. 1(b) indicates the relative strength of transitions from $(0, 5)_0$ for microwaves polarized along z . This is proportional to $|\mu_{0i}^z|^2$, where μ_{0i}^z is the z component of the transition dipole moment $\mu_{0i} = \langle 0 | \mu | i \rangle$; here $|0\rangle$ and $|i\rangle$ are the state vectors for the sublevels $(0, 5)_0$ and $(1, 5)_k$. Of the three transitions allowed for microwaves polarized along z in parallel fields, only one retains its strength as electric field increases. This is the one that is predominantly $M_N = 0$ at high field, and it correlates with $(1, 5)_2$ at zero field. By applying an electric field, we sup-

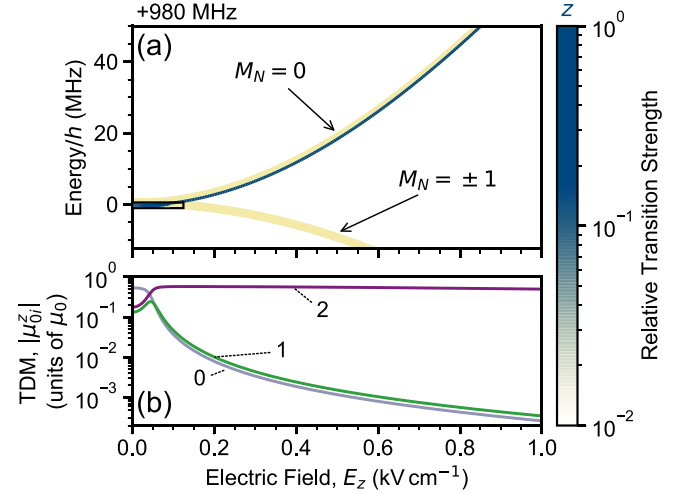


FIG. 2. (a) The energy levels of RbCs ($N = 1$) in a dc electric field and a magnetic field of 181.5 G. The relative transition strengths are shown in Fig. 1(b). (b) The transition dipole moments of the transitions $(0, 5)_0 \rightarrow (1, 5)_k$ for $k = 0, 1, 2$ [as labeled in Fig. 1(a)] as a function of the electric field.

press the effect of the nuclear spins on the internal structure as shown in Appendix, Table II.

In Fig. 2(a) we increase the electric field further to 1000 V cm $^{-1}$. The dc Stark shift is approximately quadratic; at 400 V cm $^{-1}$ only the state $(1, 5)_2$ has any appreciable transition dipole moment from $(0, 5)_0$. We show the evolution of the relative transition strength in Fig. 1(b) by shading the appropriate energy level in the Stark map; we also show the numerical values of $|\mu_{0i}^z|$ in Fig. 2(b) for the states highlighted in Fig. 1(a). Although there are 32 sublevels for each (N, M_N) , split by the nuclear Zeeman interaction, the hyperfine coupling no longer has a significant impact on the level structure for states that are predominantly $M_N = 0$. This implies that a simpler Hamiltonian can be used to explain the internal structure; for this we drop H_{hf} and H_{Zeeman} from (1) to leave a simpler hindered-rotor Hamiltonian [31,89,90]. The eigenstates of this simpler system do not depend on the nuclear spin degrees of freedom and can be constructed from the spherical harmonics alone [31,89],

$$|\psi_{\text{hindered}}\rangle = \sum_{N'} A_{N'} |N', M_N\rangle. \quad (14)$$

The application of an electric field greatly simplifies the hyperfine structure, and leads to more linear ac Stark shifts in the presence of E_{ac} . In Fig. 3 we show the shifts of the transitions with $\Delta M_F = 0$ as a function of laser intensity, with a dc magnetic field of 181.5 G, for three laser polarization angles: $\beta = 0^\circ$, β_{magic} , and 90° . Here β_{magic} is the “magic angle” that occurs at the point where $P_2(\cos \beta) = 0$, which is $\beta_{\text{magic}} \approx 54.7^\circ$ [91–93]. At this angle, the diagonal elements of (11) are reduced to zero. In Fig. 3(a) we show the ac Stark shift without an electric field. For $\beta \neq 0^\circ$, the intensity dependence is nontrivial, with a rich pattern of avoided crossings. We have previously shown that, while these avoided crossings can be used to minimize the differential ac Stark shift locally for certain transitions [94], their effectiveness in producing an

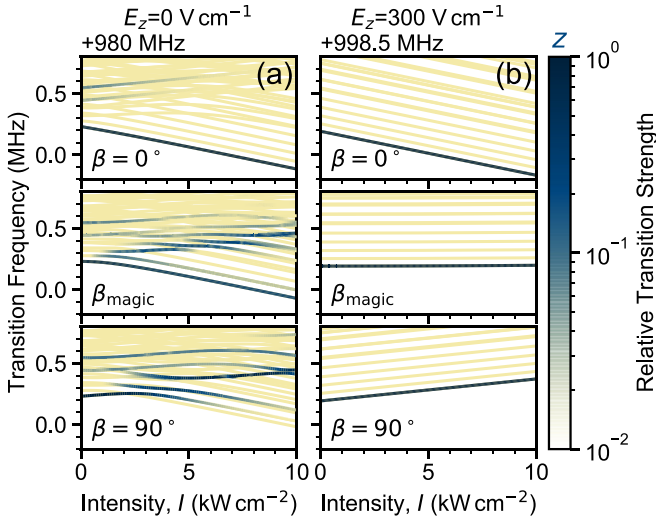


FIG. 3. Frequencies of the transitions $(0, 5)_0 \rightarrow (1, 5)_k$ in a dc magnetic field of 181.5 G, as a function of laser intensity, for three polarization angles $\beta = 0^\circ$, β_{magic} , and 90° . The relative transition strengths are coded as in Fig. 1(b). (a) At zero dc electric field. (b) At an electric field of 300 V cm^{-1} . Note the different offsets on the transition frequency axes due to the dc Stark shift. The calculations use the values of $\alpha^{(0)}$ and $\alpha^{(2)}$ determined experimentally in Sec. V.

intensity-insensitive trap is limited. In this region, the ac Stark shift can be adequately quantified only by the gradient of the transition frequency f with respect to intensity I . This gives a measure of the “local” differential polarizability, which depends strongly on intensity. We contrast this with the behavior in Fig. 3(b), where an electric field of 300 V cm^{-1} has been introduced. The states are now well represented by (14), and this leads to df/dI independent of intensity. Most importantly, df/dI can be reduced to zero at the magic angle [91–93].

The simplified internal structure is less sensitive to variation in the external trapping potential. For molecules at a temperature of $1.5 \mu\text{K}$, a suitable trap has depth $\sim k_B \times 15 \mu\text{K} \approx h \times 300 \text{ kHz}$. This depth is comparable to the hyperfine splitting, and so variations in laser intensity as molecules move around the trap can strongly change the structure. By contrast, when states with different values of $|M_N|$ are separated by more than 1 MHz, as is the case at $E_z > 100 \text{ V cm}^{-1}$, the ac Stark effect is much weaker than the energy splitting, and so sensitivity to such variations is reduced.

III. DETAILS OF THE EXPERIMENT

Our experimental apparatus and the method for creating ultracold RbCs molecules have been discussed in previous publications [40,95–99]. In this work, we create a sample of up to ~ 3000 RbCs molecules in their absolute ground state at a temperature of $1.5(1) \mu\text{K}$ by magnetoassociation on an interspecies Feshbach resonance [96], followed by transfer to the rovibronic and hyperfine ground state by stimulated Raman adiabatic passage (STIRAP) [40,99]. The magnetoassociation is performed in a crossed optical dipole trap (ODT) operating at $\lambda = 1550 \text{ nm}$, but the STIRAP is performed in free space to avoid spatially varying ac Stark shifts [98,99]. A

uniform magnetic field of 181.5 G is present following magnetoassociation and throughout the STIRAP. Once prepared in the ground state, the molecules may be recaptured in the ODT and/or interrogated with microwave fields to drive transitions to rotationally excited states [86]. Detection is performed by reversing the STIRAP and magnetoassociation steps, breaking the molecules apart into their constituent atoms, which are then imaged using conventional absorption imaging. We are therefore able to detect molecules only when they are in the specific rotational and hyperfine state addressed by STIRAP.

In this work, we consider the ac Stark shift at $\lambda = 1064 \text{ nm}$. The 1064 nm light is derived from a Nd:YAG based master-oscillator-power-amplifier (MOPA) system. We monitor the laser frequency using a HighFinesse WS-U wavemeter. The wavemeter output is used as the input to a software-based servo loop, which provides feedback to the temperature of the MOPA’s Nd:YAG crystal to stabilize the output frequency. Using this approach, we are able to stabilize the frequency of the light to $\sim 10 \text{ MHz}$ over a tuning range of $\sim 24 \text{ GHz}$. For trapping, we can split the light into two beams that form a second crossed optical trap. For our spectroscopic work we require only a single beam, which has a waist of $173(1) \mu\text{m}$; the large waist ensures that the molecules experience a nearly homogeneous intensity.

To control the rotational and hyperfine state of the molecule, we use resonant microwaves [85,86,94]. The microwaves are emitted by two omnidirectional quarter-wave antennas, tuned to the $N = 0 \rightarrow 1$ transition frequency. Each antenna consists simply of a 7.5-cm-long straight copper wire connected to a coaxial cable. The antennas are connected to two independent signal generators that are both frequency-referenced to a 10 MHz GPS signal. The microwave output can be switched on a nanosecond timescale and is controlled externally by TTL pulses synchronized to the experimental sequence. The antennas are oriented perpendicularly to each other, with one antenna mounted parallel to the direction of the magnetic field (the z axis) and the other mounted in the horizontal (x - y) plane orthogonal to the direction of the magnetic field. In free space, both antennas should produce linearly polarized microwaves, either parallel or orthogonal to the direction of the magnetic field according to the antenna orientation. In practice we find that both antennas actually generate a strong component polarized parallel to the magnetic field direction. We attribute this to the boundary conditions imposed by the presence of magnetic field coils separated by less than a quarter of the microwave wavelength.

For the generation of dc electric fields, two pairs of electrodes are mounted around the UHV fused silica cell in which the ultracold molecules are prepared [40]. The electrodes are arranged such that the electric field maximum is located at the position of the ODT. As the cell is dielectric, some remnant charge can build up on the glass. We find that limiting the maximum electric field we apply to 500 V cm^{-1} reduces the impact of the electric field variation on our spectroscopic measurements, within a single experimental run, to less than the $\sim 10 \text{ kHz}$ Fourier width associated with our square microwave pulses. Additionally, between experimental runs, high-power UV light (up to 3 W with wavelength 365 nm) irradiates the cell for 1 s, removing any accumulated charges.

IV. OPTICAL TRAPPING IN THE GROUND STATE

Theoretical analysis shows that the polarizability of RbCs in the ground vibronic state is dominated by transitions to vibrational levels of the $A^1\Sigma$ and $B^1\Pi$ states [78,101]. The potential minima of these states lie 300 and 410 THz above the vibronic ground state, respectively. This is higher in energy than the $\sim h \times 281$ THz provided by one photon with $\lambda = 1064$ nm, as shown in Fig. 5(b). It is worth noting that, due to spin-orbit coupling, the lowest levels of the $b^3\Pi$ electronic state have significant singlet character, which produces strong resonant behavior from $h \times 262$ to $h \times 270$ THz even though singlet-triplet transitions are forbidden. The calculations indicate that the polarizabilities of the ground and Feshbach molecular states vary smoothly from 270 to 300 THz (wavelengths from 1020 to 1110 nm), and predict that the difference between them crosses zero at 1064.96 nm [78]. The transitions to vibronic levels of the $b^3\Pi$ state in this wavelength range are suppressed by negligible Franck-Condon factors [78,101]. Nevertheless, during initial attempts to load RbCs molecules into an ODT of $\lambda \approx 1064$ nm, we observed a loss of ground-state molecules that was orders of magnitude faster than the near-universal collisional losses that typically dominate our experiments [102,103].

To investigate the optical losses, we trap ground-state molecules in the crossed optical dipole trap at $\lambda = 1550$ nm and pulse on the light at $\lambda = 1064$ nm in a single beam to perform spectroscopy. We find that the loss of molecules is very sensitive to laser frequency, with several resonances in the region accessible to us. To determine the nature of these resonances, we designate one of the resonant frequencies $f_0 = 281.634\,630(2)$ THz, and we stabilize the laser to this frequency; we apply additional modulation of 35 MHz at a rate of 5 kHz to remove error due to frequency tuning. We measure the loss of molecules as a function of time due to the resonant light. Example loss measurements are shown in Fig. 4(a).

We examine the density dependence of the loss by reducing the starting number of ground-state molecules while keeping all other experimental parameters the same. Figure 4(b) shows the rate of change of the fraction remaining, over the first 15 ms, for two samples with a factor of 2 difference in the initial density; this is the largest change that we can make while still being able to measure an accurate lifetime. The two measurements agree within one standard deviation, so we conclude that the resonant loss is principally a one-body process.

To investigate the mechanism behind the resonant loss, we model the rate of change of density n as

$$\dot{n}(r, t) = -k_2 n(r, t)^2 - k_1 n(r, t). \quad (15)$$

We fix the rate coefficient for two-body inelastic loss $k_2 = 4.8 \times 10^{-11} \text{ cm}^3 \text{ s}^{-1}$ at the value measured previously [102], and we extract the rate coefficient k_1 for resonant loss. We measure k_1 as a function of the peak intensity of the beam at $\lambda = 1064$ nm. The results are shown in Fig. 4(c). We fit the resulting variation with the function $k_1 = AI^\kappa$, with A as a free parameter. We fix $\kappa = 1, 2, 3$ corresponding to loss due to a one-, two-, or three-photon process, and we find $\chi_{\text{red}}^2 = 31, 4$, and 17, respectively. We confirm this fitting by additionally allowing κ to vary: we find $\kappa = 2.02(8)$ with no significant

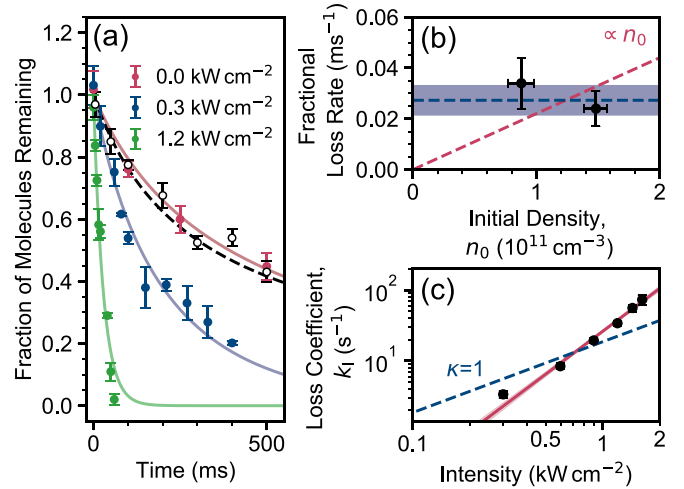


FIG. 4. Molecular loss in light of wavelength $\lambda = 1064$ nm. (a) Molecule loss as a function of time for various laser intensities. The filled points show resonant loss at laser frequency f_0 ; an additional dipole trap with $\lambda = 1550$ nm is used for confinement. For the unfilled black points the laser is detuned by -12.3 GHz, and the intensity is increased to 11.2 kW cm^{-2} without the dipole trap at 1550 nm. (b) Fractional loss rate over the first 15 ms as a function of initial peak density for laser frequency f_0 . The dashed lines indicate the scaling expected for one-molecule (blue) and two-molecule (red) processes. (c) Rate coefficient for resonant loss (k_1) as a function of laser intensity (I). The solid line shows a fit of the form $k_1 \propto I^\kappa$, which yields a best-fit value of $\kappa = 2.02(8)$; the shaded region indicates the error on the fit. The dashed line shows the scaling expected for a one-photon process.

change in the best value for χ_{red}^2 . We conclude that the loss is a two-photon process, with $A_{\gamma=2} = 25(1) \text{ s}^{-1} (\text{kW cm}^{-2})^{-2}$.

The resonant loss is a one-body process with quadratic dependence on intensity. We believe it is caused by driving one or more two-photon transitions to an electronically excited state. A pair of photons with $\lambda = 1064$ nm has sufficient energy to drive transitions to the low-lying levels of the $(5)^1\Sigma^+$ state; its potential curve, shown in Fig. 5(b), has a minimum of energy $h \times 557$ THz ($\lambda = 538$ nm) above that of the ground state [100,104]. We can suppress the resonant loss, such that it becomes unobservable in our experiments, by tuning the laser frequency several GHz away from the transition. By doing this, we have been able to load RbCs molecules into an ODT made with 1064 nm light, with the lifetime limited by optical excitation of complexes formed in bimolecular collisions [102,103,105].

To resolve transitions, we reduce the intensity to $\sim 1 \text{ kW cm}^{-2}$ and dither the frequency over 35 MHz, pulsing the light on for 50 ms. The dithering artificially broadens the transitions to the level where we can resolve individual lines with our current apparatus. In Fig. 5(a) we show the resulting spectra. We fit the observed lines with a Gaussian function to extract center frequencies with uncertainties of a few MHz. From the $(0, 5)_0$ sublevel of $N = 0$ we observe two doublets with the strongest components at laser frequencies f_0 and $f_0 + 1.189(3)$ GHz. This energy splitting is typical for rotational transitions.

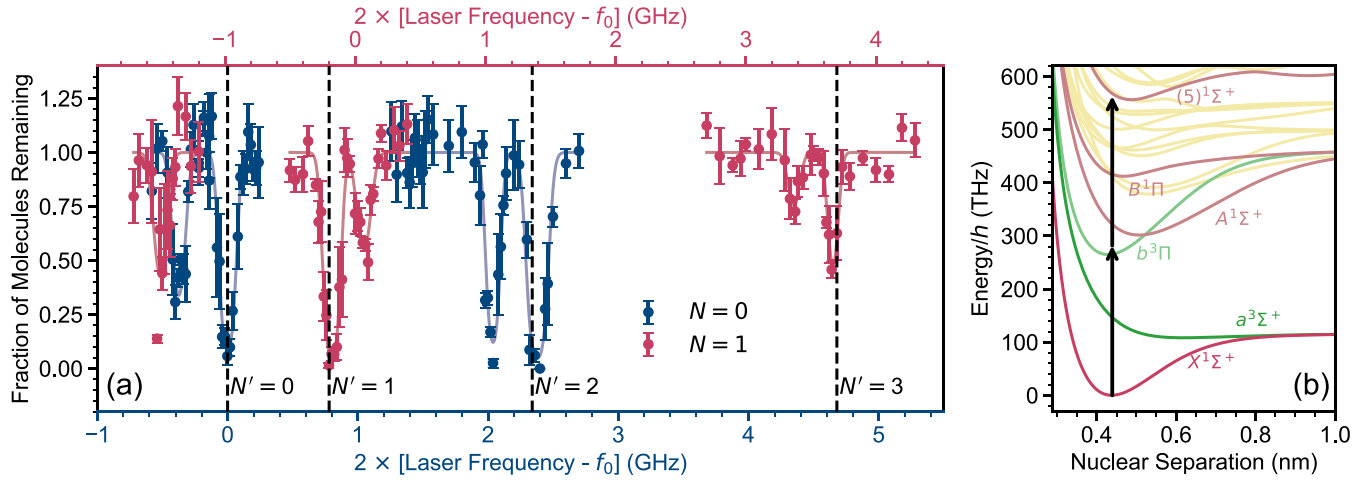


FIG. 5. Resonant two-photon loss of ground-state molecules in the presence of light with $\lambda = 1064$ nm. (a) The fraction of molecules trapped with light at $\lambda = 1550$ nm that remain after exposure to light with $\lambda = 1064$ nm, as a function of laser frequency. Measurements are shown for molecules prepared in $N = 0$ (blue) or $N = 1$ (red). To display the results on a continuous scale corresponding to the excited-state energy, we plot the horizontal axes as twice the laser frequency [offset from $f_0 = 281,634.630(2)$ GHz] and offset the measurements for $N = 1$ by $2 \times B_{v=0}/h = 980.231$ MHz on the top axis. Each data point is the average of three runs, with error bars indicating the standard deviation; the solid lines are Gaussian fits to the data. The vertical dashed lines indicate the excited-state rotational structure for $B'_v = h \times 389.9(4)$ MHz. (b) The potential energy curves for low-lying electronic states of RbCs [100]. The black arrows indicate the energies of one- and two-photon transitions at $\lambda = 1064$ nm.

To ensure that we can reliably trap rotationally excited molecules, we repeat the loss spectroscopy for molecules that have been transferred to the $(1, 5)_0$ sublevel of $N = 1$ by a microwave π -pulse [86]. The results are shown in Fig. 5, offset by the microwave transition frequency 980.231 MHz. From this state we see markedly different structure, with two doublets and a singlet. The strongest components of the two doublets are at laser frequencies $f_0 - 0.0903(17)$ GHz and $f_0 + 1.834(3)$ GHz. The singlet is at $f = f_0 - 0.749(6)$ GHz.

We believe that the lines observed are probably due to two-photon transitions of the form $X^1\Sigma, v = 0, N \rightarrow (5)^1\Sigma, v', N'$. The rotational selection rule for a two-photon transition is $\Delta N = 0, \pm 2$. We fit the strongest of each pair of lines in the spectra to the eigenvalues of the rotational Hamiltonian $B'_v N'(N' + 1)$, weighted by the error in the center frequencies extracted from the fits. This gives $B'_v = h \times 389.9(4)$ MHz, which compares favorably with the theoretical value of 410 MHz [100], calculated at the potential minimum of the $(5)^1\Sigma$ state.

V. DETERMINING THE POLARIZABILITY

A. Isotropic polarizability in the ground state

As described in Sec. II, the isotropic part of the polarizability, $\alpha^{(0)}$, produces an equal energy shift of all $(N, M_F)_k$ while the term proportional to $\alpha^{(2)}$ is nonzero only for $N > 0$. Thus only $\alpha^{(0)}$ contributes to the trapping potential for $N = 0$. The value of this component can be found either by direct trap frequency measurements, e.g., through parametric heating [85], or by the differential ac Stark shift between two vibronic states. We choose the second method and measure the intensity-dependent energy shift of the ground state with respect to a weakly bound Feshbach state. In Fig. 6 we show the two-photon transition used in STIRAP [98], measured

with and without the light of wavelength 1064 nm. Hereafter, we refer to this light as the “trapping light,” even when its intensity is too low to form an actual trap. It is delivered in a single beam with a waist of 173(1) μm and peak intensity of 8.60(7) kW cm^{-2} .

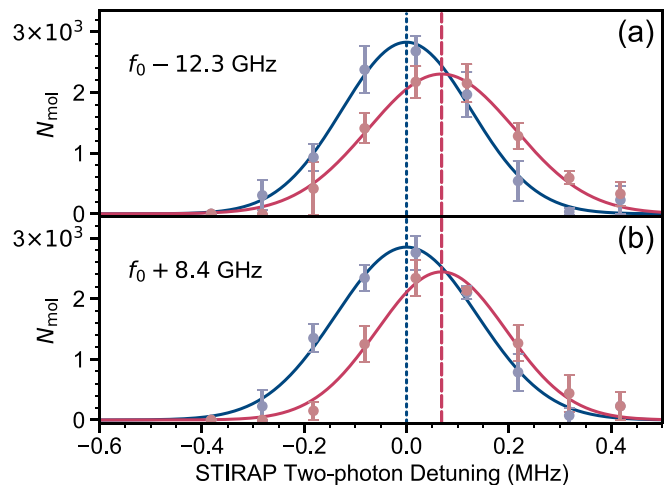


FIG. 6. Measurement of the polarizability of RbCs in the rovibronic ground state, using the ac Stark shift of the two-photon STIRAP resonance (a) with the laser tuned 12.3 GHz below the resonance at f_0 shown in Fig. 5(a); (b) with the laser tuned 8.4 GHz above the resonance. The blue points are measured in free space while the red points are measured with the 1064 nm laser at an intensity of 8.60(7) kW cm^{-2} . The vertical dashed lines indicate the centers of the fits. The shifts for the two detunings agree within experimental error, indicating that there is no impact from the two-photon transitions in Fig. 5.

Two-photon transitions might produce a term in the Hamiltonian proportional to I^2 , corresponding to a fourth-order hyperpolarizability. To ascertain whether such effects are significant, we perform measurements with the trapping laser tuned approximately ± 10 GHz from the loss features observed in Fig. 5. The energy shifts measured above and below the transitions are $h \times 68(8)$ kHz and $h \times 68(9)$ kHz, respectively. These identical shifts confirm that the laser frequency is far from resonance with the two-photon transitions.

The measured energy shift gives the difference in polarizability between the ground and Feshbach states. The molecule's constituent atoms interact very weakly in the Feshbach state, so its polarizability is just the sum of the atomic polarizabilities α_{Rb} and α_{Cs} , which are well known [106]. The weighted average of our two measurements yields the polarizability of the rovibronic ground state. Because of rotational averaging, this is equivalent to the isotropic polarizability of the ground vibronic state,

$$\begin{aligned}\alpha^{(0)} &= \alpha_{\text{Rb}} + \alpha_{\text{Cs}} + 4\pi\epsilon_0 \times 1.7(4) \times 10^2 a_0^3 \\ &= 4\pi\epsilon_0 \times 2.02(4) \times 10^3 a_0^3.\end{aligned}$$

Our measurement corresponds to a ratio of the ground-state and Feshbach polarizabilities [$\alpha^{(0)}/(\alpha_{\text{Rb}} + \alpha_{\text{Cs}})$] of 1.09(2). This is significantly different from the value of 1.000 06 predicted by Vexiau *et al.* [78]. Our previous work [85] at a wavelength of 1550 nm found good agreement between the experimental ratio of 0.88(1) and the predicted value of 0.874. The difference observed here may arise because the polarizability at $\lambda = 1550$ nm is dominated by far-detuned transitions to the $A^1\Sigma$ state, whereas $\lambda = 1064$ nm is closer to resonance and the polarizability is more sensitive to the frequencies and strengths of individual transitions.

B. Anisotropic polarizability

In this section, we determine the value of the anisotropic polarizability, $\alpha^{(2)}$. We use microwave spectroscopy of the $N = 0 \rightarrow 1$ rotational transition in RbCs, with an applied magnetic field of 181.5 G. The measurements in the previous subsection are insensitive to $\alpha^{(2)}$, because it does not affect trapping in the rotational ground state. However, $\alpha^{(2)}$ is always important for $N > 0$. Moreover, states with permanent laboratory-frame dipole moments always involve mixtures of rotational states, and so $\alpha^{(2)}$ is needed whenever an electric field is applied.

We measure the value of $\alpha^{(2)}$ for RbCs at $\lambda = 1064$ nm by considering the frequency shift of the rotational transitions as a function of laser intensity. In Fig. 7 we show the ac Stark maps for $\beta = 0^\circ$ and 90° . The mixing of hyperfine states causes complex patterns of crossings and avoided crossings. We calculate these patterns by diagonalizing the full Hamiltonian of (1)–(11). We fit simultaneously to the experimental microwave spectra for $\beta = 0^\circ$ and 90° and obtain a good fit with the single value $\alpha^{(2)}/4\pi\epsilon_0 = 1997(6) a_0^3$. This contrasts with previous work [85] at $\lambda = 1550$ nm that required separate values of $\alpha^{(2)}$ at $\beta = 0^\circ$ and 90° .

With knowledge of both parts of the polarizability, we have determined all the parameters in both the full hyperfine

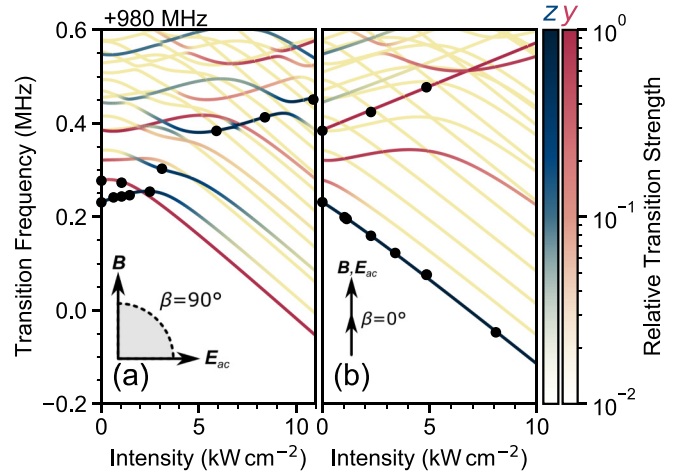


FIG. 7. Frequencies of the transitions from $(0, 5)_0$ to hyperfine sublevels of $N = 1$ in a dc magnetic field of 181.5 G, as a function of laser intensity, for laser polarization angle (β) (a) perpendicular to and (b) parallel to the uniform 181.5 G magnetic field. Each point is the fitted center frequency from a measured microwave spectrum; the uncertainties are a few kHz, which is too small to be seen at this scale. The relative transition strengths for microwaves polarized along z and y are shown as blue and red color maps, respectively.

and hindered-rotor Hamiltonians described in Sec. II. Accordingly, all results in the remainder of the paper are presented without free parameters.

VI. CONTROLLING THE ac STARK EFFECT

A. In a magnetic field

We first investigate the effect of the polarization of the trapping light on the ac Stark effect in the absence of an electric field. We fix the intensity of the trapping light at $1.05(1) \text{ kW cm}^{-2}$ and vary the polarization angle. Figure 8(a) shows the polarization-dependent Stark shift at (i) 181.5 G and (ii) 355 G. In both cases, the ac Stark shift deviates from the form proportional to $P_2(\cos \beta)$ expected from models that ignore hyperfine structure; the frequency shift actually crosses zero at $\beta = 63(1)^\circ$. To investigate the intensity dependence at this zero crossing, we fix the polarization at this angle and vary the intensity at both magnetic fields; these measurements are shown in Fig. 8(b). In both cases, the light shift shows a maximum as a function of intensity and crosses zero with substantial gradient.

The results in Fig. 8 indicate that hyperfine effects play a significant role in the ac Stark effect under these conditions. The hyperfine interactions mix states with different values of M_N in (13), so that the ac Stark effect has a different dependence on angle. It is expected that, at higher magnetic fields, the nuclear spins will decouple from the rotational angular momentum. However, this does not happen for RbCs at the magnetic fields we use; this is unsurprising in view of the small magnetic moments in the molecule, compared to the hyperfine structure and ac Stark effect. Our calculations including hyperfine structure show that the field would need to be ~ 700 G for the $|N = 1, M_N = 0, m_{\text{Rb}} = 3/2, m_{\text{Cs}} = 7/2\rangle$ component of the state $(1, 5)_0$ to be greater than 99%.

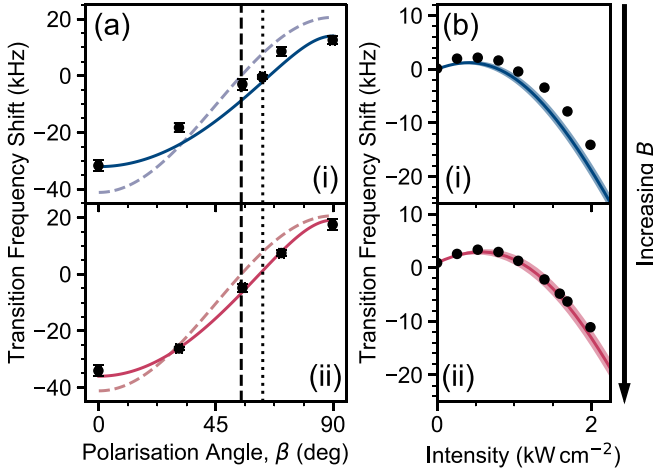


FIG. 8. The anisotropic light shift of the transition $(0, 5)_0 \rightarrow (1, 5)_0$ in a magnetic field of (i) 181.5 G and (ii) 355 G as a function of (a) polarization angle β , for a fixed laser intensity of $1.05(1) \text{ kW cm}^{-2}$ and (b) laser intensity, with β set to the zero crossing measured in (a), as indicated by the dotted line. Each point is the fitted center frequency from a measured microwave spectrum; the uncertainties are a few kHz. The solid lines are calculated from the full Hamiltonian, including the hyperfine and Zeeman structure. The shaded regions in (b) indicate the $\pm 1^\circ$ uncertainty in setting the polarization angle to the zero crossing. The colored dashed line shows the result of the hyperfine-free hindered-rotor Hamiltonian, with the vertical dashed line indicating the position of the associated zero crossing.

B. In combined electric and magnetic fields

In the molecular frame, RbCs has a permanent electric dipole moment of 1.23 D. Because of this, there is stronger coupling to dc electric fields than to a dc magnetic field. A modest electric field is sufficient to decouple the rotational and nuclear angular momenta. In Fig. 9 we show the calculated Stark shifts and relative strengths of the microwave transitions from the state $(0, 5)_0$ over a similar electric field range to Fig. 2(a) again for a magnetic field of 181.5 G. A field of 100 V cm^{-1} is sufficient to split the $N = 1$ rotational level into two branches with $M_N = 0$ and ± 1 and to reach 99% state purity for $(1, 5)_2$.

In Fig. 10(a) we show the polarization dependence of the ac Stark shift in a dc electric field of 300 V cm^{-1} , using a fixed intensity of 3.12 kW cm^{-2} . In this case, the measured points agree within one standard deviation with the results of the hyperfine-free hindered-rotor Hamiltonian, using the previously measured value of $\alpha^{(2)}$. This shows that even a modest electric field can decouple N , i_{Rb} , and i_{Cs} .

To test the remaining ac Stark shift, we fix the polarization angle β of the trapping laser to the magic angle of 54.7° and vary the intensity of the light. The results are shown in Fig. 10(b) for three electric fields. We see that the ac Stark shift scales approximately as I^2 ; this phenomenon is often termed “hyperpolarizability,” but it is important to recognize that it is completely described within (11), which includes only electronic polarizability and not electronic hyperpolarizability. At higher electric fields, the effect of $\alpha^{(2)}$ is reduced; at 300 V cm^{-1} the maximum frequency shift due to $\alpha^{(2)}$ is

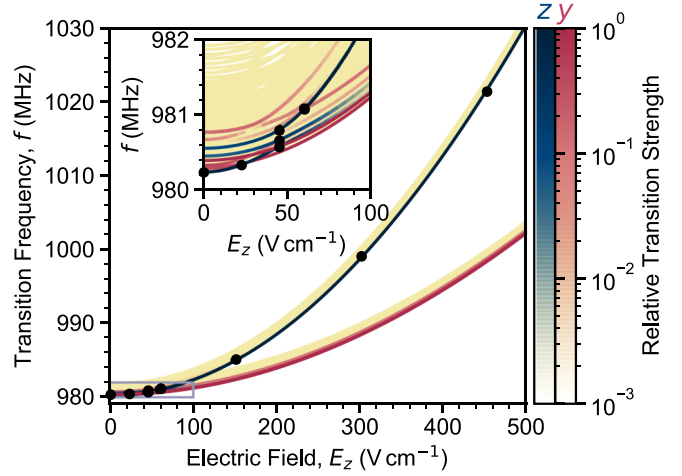


FIG. 9. The dc Stark shift of transitions from $(0, 5)_0$ to hyperfine sublevels of $N = 1$ as a function of electric field with a 181.5 G magnetic field. The inset shows the highlighted region at low electric field. The relative transition strengths for microwaves polarized along z and y are coded as in Fig. 7. Each point is the fitted center frequency from a measured microwave spectrum; the uncertainties are a few kHz, which is too small to be seen at this scale. At higher electric fields, the energy levels for $N = 1$ are split into branches with $M_N = 0$ and $|M_N| = 1$. In the high-field limit, only one transition can be driven with microwaves polarized along z . At lower fields, hyperfine mixing allows multiple transitions; this can be seen clearly at $E_z \lesssim 50 \text{ V cm}^{-1}$.

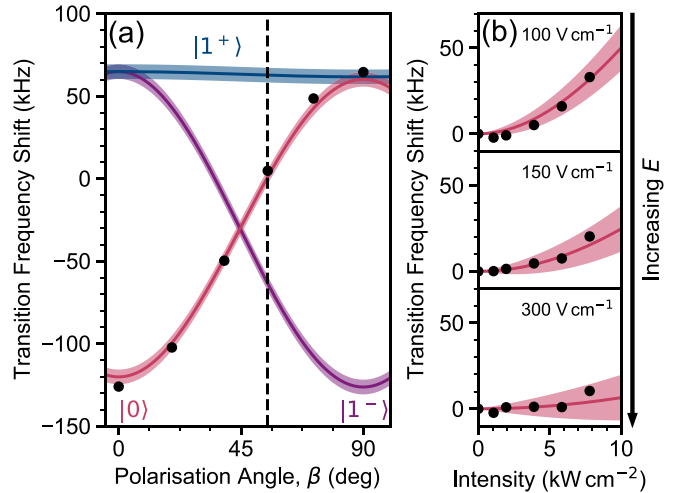


FIG. 10. The ac Stark shifts of transitions $N = 0 \rightarrow N = 1$ with a dc electric field along the uniform 181.5 G magnetic field. The shifts are shown as a function of (a) the polarization angle (β) of the trapping laser with an electric field of 300 V cm^{-1} and a laser intensity of 3.12 kW cm^{-2} ; and (b) the laser intensity with β fixed to the magic angle [indicated in (a) by the dashed line]. Each point is the fitted center frequency from a measured microwave spectrum for the $(0, 5)_0 \rightarrow (1, 5)_2$ line; the uncertainties are a few kHz, which is too small to be seen at this scale. The solid lines show the results of the hyperfine-free hindered-rotor Hamiltonian. The lines are labeled with $|M_N|$ for $N = 1$; the ac Stark term mixes states with $M_N = \pm 1$, and the resulting combinations are labeled 1^\pm . The shaded regions indicate the error due to the uncertainty in $\alpha^{(2)}$, though the scatter in the experimental points is dominated by electric field noise.

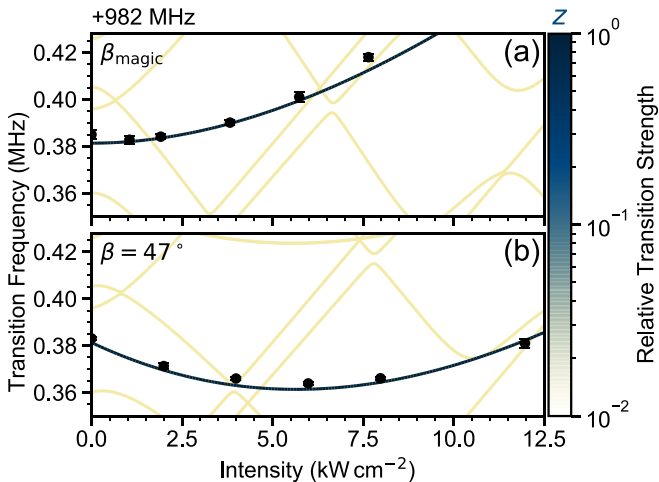


FIG. 11. The ac Stark shift of the transition $(0, 5)_0 \rightarrow (1, 5)_2$ in an electric field of 100.8 V cm^{-1} as a function of the intensity of the trapping laser. The shifts are shown for two values of the polarization angle, β . Each point is the fitted center frequency from a measured microwave spectrum; the uncertainties are a few kHz. The continuous lines are the results from the full Hamiltonian including hyperfine and Zeeman terms. Transition strengths for microwaves polarized along z are coded as in Fig. 8.

$10.0(1.6) \text{ kHz}$, although that due to the dc Stark effect is $\sim 20 \text{ MHz}$. This simplified ac Stark shift comes at the cost of increased sensitivity to electric field noise, which we believe is at the level of one part in a thousand in the present experiments, and is responsible for the remaining scatter in Fig. 10(b).

C. Beyond the magic angle

At the magic angle, $\beta_{\text{magic}} \approx 54.7^\circ$, the diagonal terms of (11) are zero. In a state that is well described by a single basis function $|N = 1, M_N\rangle$, this removes the component of the ac Stark shift due to $\alpha^{(2)}$. However, due to the quadratic intensity dependence of the remnant ac Stark shift, as seen in Figs. 10(b) and 11(a), the differential polarizability is reduced to zero at $I = 0$. Here we describe a tunable arrangement in which the total frequency shift is reduced to near zero at an intensity suitable for trapping. This technique does not require full decoupling of the nuclear spins from the rotation, so it can be used at much smaller electric fields, reducing the sensitivity to electric field noise.

In Fig. 11 we compare the ac Stark shifts of the $(N = 0, M_N = 0) \rightarrow (1, 0)$ transition at two different polarization angles with the results of the full Hamiltonian including hyperfine structure. At β_{magic} , shown in Fig. 11(a), the ac Stark shift increases almost quadratically with intensity. However, by tuning the polarization angle away from β_{magic} we can engineer a broad minimum at a required intensity; for $I \approx 6 \text{ kW cm}^{-2}$ this occurs at $\beta = 47^\circ$, as seen in Fig. 11(b). This intensity corresponds to a trap depth of $27 \text{ } \mu\text{K}$ in the rotational ground state, so it would be suitable for trapping molecules at our current molecular temperature of $1.5 \text{ } \mu\text{K}$.

We quantify the expected transition frequency spread Δf for a 4% spread in intensity by evaluating the Taylor ex-

pansion of the ac Stark map at $I = I_0$ and $I_0 - \Delta I$ for the two cases shown in Fig. 11. For $\beta = 54.7^\circ$ we obtain $\Delta f = 1.5 \text{ kHz}$. By contrast, for $\beta = 47^\circ$, where we have optimized the intensity to minimize differential Stark shifts, we obtain $\Delta f = 33 \text{ Hz}$. The coherence time in this arrangement should scale with $1/\Delta f \sim 30 \text{ ms}$. For comparison, Neyenhuis *et al.* [92] achieved a rotational coherence time of $1.5(2) \text{ ms}$ by tuning the angle of the laser polarization to a zero crossing in the differential ac Stark shift. More recently, Seeßelberg *et al.* [93] trapped $^{23}\text{Na}^{40}\text{K}$ in an electric field in a spin-decoupled optical lattice and observed a coherence time of $8.7(6) \text{ ms}$.

VII. OUTLOOK AND SUMMARY

In this work, we have characterized the behavior of the RbCs molecule in light of wavelength 1064 nm . We have found that the lifetime of the molecule in traps of this wavelength can be severely impacted by two-photon transitions to the $(5)\Sigma^+$ state. However, there are regions between these transitions where the losses are not significantly enhanced. We have determined the isotropic polarizability of the molecule in these regions with optical spectroscopy of the rovibronic ground state. We have also found the anisotropic polarizability by observing the ac Stark effect on hyperfine components of the $N = 0 \rightarrow 1$ rotational transition using microwave spectroscopy with kHz precision.

We have studied the impact of applying additional dc electric and magnetic fields on the ac Stark shift. A magnetic field beyond our current experimental capability would be required to reduce the impact of the hyperfine structure. However, we have found that a modest electric field is sufficient to decouple the rotational motion from the nuclear spins and simplify the hyperfine structure. Under these circumstances, we can model the structure using a hindered-rotor Hamiltonian, without hyperfine or Zeeman terms.

Our medium-term goal is to achieve long coherence times for molecules in optical lattices and tweezers. To achieve this, we need to reduce the dependence of the ac Stark shift on laser intensity, at intensities high enough for trapping. We have found that this may be achieved for RbCs by applying a moderate dc electric field and adjusting the polarization angle of the laser. The optimum polarization angle is close to the magic angle of 54.7° for low laser intensities, but different polarization angles are needed at the higher intensities necessary for trapping. This result paves the way to using arrays of RbCs molecules as a platform for quantum simulation.

ACKNOWLEDGMENTS

This work was supported by U.K. Engineering and Physical Sciences Research Council (EPSRC) Grants No. EP/P01058X/1 and No. EP/P008275/1. The data, code, and analysis associated with this work are available in Ref. [107]. The python code for hyperfine structure calculations can be found in Ref. [108].

APPENDIX: HYPERFINE STATE COMPOSITION

In the main body of the paper, we consider the rotational and hyperfine states of RbCs at a magnetic field of 181.5 G .

TABLE I. The state compositions of the state with $M_F = 5$ and $N = 0, 1$ in a magnetic field of 181.5 G. The calculations are performed in the uncoupled basis with basis states $|N, M_N, m_{\text{Rb}}, m_{\text{Cs}}\rangle$, and they have been rounded to one part in 10^3 . Components not shown are zero to this level of precision. The bold component is the state that is adiabatically connected at high magnetic field.

State $(N, M_F)_k$	Composition in the $ N, M_N, m_{\text{Rb}}, m_{\text{Cs}}\rangle$ basis
$(0, 5)_0$	$0, 0, 3/2, 7/2\rangle$
$(1, 5)_0$	$0.087 1, 1, 3/2, 5/2\rangle - 0.371 1, 1, 1/2, 7/2\rangle$ $+ 0.925 1, 0, 3/2, 7/2\rangle$
$(1, 5)_1$	$0.905 1, 1, 3/2, 5/2\rangle - 0.358 1, 1, 1/2, 7/2\rangle$ $+ 0.229 1, 0, 3/2, 7/2\rangle$
$(1, 5)_2$	$0.416 1, 1, 3/2, 5/2\rangle + 0.857 1, 1, 1/2, 7/2\rangle$ $+ 0.304 1, 0, 3/2, 7/2\rangle$

At this magnetic field, the good quantum numbers are the rotational quantum number N and the projection M_F of the total angular momentum. Because these quantum numbers do not uniquely identify individual hyperfine sublevels, we label each by $(N, M_F)_k$, where k is an index, starting at $k = 0$, that counts up in energy at 181.5 G for states with the same values of N and M_F . In this Appendix, we present the state composition of the hyperfine sublevels ($N = 1, M_F = 5$) $_k$ for two values of the electric field: $E = 0 \text{ V cm}^{-1}$ (Table I) and $E = 300 \text{ V cm}^{-1}$ (Table II). We calculate the state composition in the uncoupled basis with basis states $|N, M_N, m_{\text{Rb}}, m_{\text{Cs}}\rangle$, where M_N is the projection of N onto the magnetic field axis and m_{Rb} and m_{Cs} are the projections of the ^{87}Rb and ^{133}Cs

TABLE II. The state compositions of the states with $M_F = 5$ and $N = 0, 1$ in a magnetic field of 181.5 G and an electric field of 300 V cm^{-1} . The calculations are performed in the uncoupled basis with basis states $|N, M_N, m_{\text{Rb}}, m_{\text{Cs}}\rangle$, and they have been rounded to one part in 10^3 . Components not shown are zero to this level of precision.

State $(N, M_F)_k$	Composition in the $ N, M_N, m_{\text{Rb}}, m_{\text{Cs}}\rangle$ basis
$(0, 5)_0$	$0.994 0, 0, 3/2, 7/2\rangle$ $+ 0.107 1, 0, 3/2, 7/2\rangle$ $+ 0.004 2, 0, 3/2, 7/2\rangle$
$(1, 5)_0$	$-0.001 0, 0, 3/2, 7/2\rangle$ $+ 0.812 1, 1, 3/2, 5/2\rangle - 0.583 1, 1, 1/2, 7/2\rangle$ $+ 0.006 1, 0, 3/2, 7/2\rangle$ $+ 0.034 2, 1, 3/2, 5/2\rangle - 0.025 1, 1, 1/2, 7/2\rangle$ $+ 0.001 3, 1, 3/2, 5/2\rangle$
$(1, 5)_1$	$0.001 0, 0, 3/2, 7/2\rangle$ $+ 0.583 1, 1, 3/2, 5/2\rangle + 0.812 1, 1, 1/2, 7/2\rangle$ $- 0.008 1, 0, 3/2, 7/2\rangle$ $+ 0.025 2, 1, 3/2, 5/2\rangle - 0.034 1, 1, 1/2, 7/2\rangle$ $+ 0.001 3, 1, 1/2, 7/2\rangle$
$(1, 5)_2$	$-0.107 0, 0, 3/2, 7/2\rangle$ $+ 0.01 1, 1, 1/2, 7/2\rangle + 0.993 1, 0, 3/2, 7/2\rangle$ $- 0.049 2, 0, 3/2, 7/2\rangle$ $+ 0.001 3, 0, 3/2, 7/2\rangle$

nuclear spins onto the magnetic field axis. The Hamiltonian used is given in the main text (Sec. II A), and the values of the relevant molecular constants are tabulated by Gregory *et al.* [86].

- [1] T. Zelevinsky, S. Kotochigova, and J. Ye, Precision Test of Mass-Ratio Variations with Lattice-Confined Ultracold Molecules, *Phys. Rev. Lett.* **100**, 043201 (2008).
- [2] J. J. Hudson, D. M. Kara, I. J. Smallman, B. E. Sauer, M. R. Tarbutt, and E. A. Hinds, Improved measurement of the shape of the electron, *Nature (London)* **473**, 493 (2011).
- [3] E. J. Salumbides, G. D. Dickenson, T. I. Ivanov, and W. Ubachs, QED Effects in Molecules: Test on Rotational Quantum States of H_2 , *Phys. Rev. Lett.* **107**, 043005 (2011).
- [4] E. J. Salumbides, J. C. J. Koelemeij, J. Komasa, K. Pachucki, K. S. E. Eikema, and W. Ubachs, Bounds on fifth forces from precision measurements on molecules, *Phys. Rev. D* **87**, 112008 (2013).
- [5] S. Schiller, D. Bakalov, and V. I. Korobov, Simplest Molecules as Candidates for Precise Optical Clocks, *Phys. Rev. Lett.* **113**, 023004 (2014).
- [6] The ACME Collaboration, J. Baron, W. C. Campbell, D. DeMille, J. M. Doyle, G. Gabrielse, Y. V. Gurevich, P. W. Hess, N. R. Hutzler, E. Kirilov, I. Kozyryev, B. R. O'Leary, C. D. Panda, M. F. Parsons, E. S. Petrik, B. Spaun, A. C. Vutha, and A. D. West, Order of magnitude smaller limit on the electric dipole moment of the electron, *Science* **343**, 269 (2014).
- [7] D. Hanneke, R. A. Carollo, and D. A. Lane, High sensitivity to variation in the proton-to-electron mass ratio in O_2^+ , *Phys. Rev. A* **94**, 050101(R) (2016).
- [8] W. B. Cairncross, D. N. Gresh, M. Grau, K. C. Cossel, T. S. Roussy, Y. Ni, Y. Zhou, J. Ye, and E. A. Cornell, Precision Measurement of the Electron's Electric Dipole Moment Using Trapped Molecular Ions, *Phys. Rev. Lett.* **119**, 153001 (2017).
- [9] M. Borkowski, Optical Lattice Clocks with Weakly Bound Molecules, *Phys. Rev. Lett.* **120**, 083202 (2018).
- [10] The ACME Collaboration, Improved limit on the electric dipole moment of the electron, *Nature (London)* **562**, 355 (2018).
- [11] M. Borkowski, A. A. Buchachenko, R. Ciuryło, P. S. Julienne, H. Yamada, Y. Kikuchi, Y. Takasu, and Y. Takahashi, Weakly bound molecules as sensors of new gravitylike forces, *Sci. Rep.* **9**, 14807 (2019).
- [12] R. V. Krems, Cold controlled chemistry, *Phys. Chem. Chem. Phys.* **10**, 4079 (2008).
- [13] M. T. Bell and T. P. Softley, Ultracold molecules and ultracold chemistry, *Mol. Phys.* **107**, 99 (2009).
- [14] S. Ospelkaus, K.-K. Ni, D. Wang, M. H. G. de Miranda, B. Neyenhuis, G. Quémener, P. S. Julienne, J. L. Bohn, D. S. Jin, and J. Ye, Quantum-state controlled chemical reactions of ultracold potassium-rubidium molecules, *Science* **327**, 853 (2010).
- [15] O. Dulieu, R. Krems, M. Weidemüller, and S. Willitsch, Physics and chemistry of cold molecules, *Phys. Chem. Chem. Phys.* **13**, 18703 (2011).

- [16] N. Balakrishnan, Perspective: Ultracold molecules and the dawn of cold controlled chemistry, *J. Chem. Phys.* **145**, 150901 (2016).
- [17] M.-G. Hu, Y. Liu, D. D. Grimes, Y.-W. Lin, A. H. Gheorghe, R. Vexiau, N. Bouloufa-Maafa, O. Dulieu, T. Rosenband, and K.-K. Ni, Direct observation of bimolecular reactions of ultracold KRb molecules, *Science* **366**, 1111 (2019).
- [18] L. Santos, G. V. Shlyapnikov, P. Zoller, and M. Lewenstein, Bose-Einstein Condensation in Trapped Dipolar Gases, *Phys. Rev. Lett.* **85**, 1791 (2000).
- [19] K.-K. Ni, S. Ospelkaus, D. J. Nesbitt, J. Ye, and D. S. Jin, A dipolar gas of ultracold molecules, *Phys. Chem. Chem. Phys.* **11**, 9626 (2009).
- [20] L. D. Carr, D. DeMille, R. V. Krems, and J. Ye, Cold and ultracold molecules: science, technology and applications, *New J. Phys.* **11**, 055049 (2009).
- [21] M. A. Baranov, M. Dalmonte, G. Pupillo, and P. Zoller, Condensed matter theory of dipolar quantum gases, *Chem. Rev.* **112**, 5012 (2012).
- [22] L. D. Marco, G. Valtolina, K. Matsuda, W. G. Tobias, J. P. Covey, and J. Ye, A Fermi degenerate gas of polar molecules, *Science* **363**, 853 (2018).
- [23] R. Barnett, D. Petrov, M. Lukin, and E. Demler, Quantum magnetism with Multicomponent Dipolar Molecules in an Optical Lattice, *Phys. Rev. Lett.* **96**, 190401 (2006).
- [24] A. Micheli, G. K. Brennen, and P. Zoller, A toolbox for lattice-spin model with polar molecules, *Nat. Phys.* **2**, 341 (2006).
- [25] H. P. Büchler, E. Demler, M. Lukin, A. Micheli, N. Prokof'ev, G. Pupillo, and P. Zoller, Strongly Correlated 2d Quantum Phases with Cold Polar Molecules: Controlling the Shape of the Interaction Potential, *Phys. Rev. Lett.* **98**, 060404 (2007).
- [26] A. Macià, D. Hufnagl, F. Mazzanti, J. Boronat, and R. E. Zillich, Excitations and Stripe Phase Formation in a Two-Dimensional Dipolar Bose Gas with Tilted Polarization, *Phys. Rev. Lett.* **109**, 235307 (2012).
- [27] S. R. Manmana, E. M. Stoudenmire, K. R. A. Hazzard, A. M. Rey, and A. V. Gorshkov, Topological phases in ultracold polar-molecule quantum magnets, *Phys. Rev. B* **87**, 081106(R) (2013).
- [28] A. V. Gorshkov, K. R. A. Hazzard, and A. M. Rey, Kitaev honeycomb and other exotic spin models with polar molecules, *Mol. Phys.* **111**, 1908 (2013).
- [29] D. DeMille, Quantum Computation with Trapped Polar Molecules, *Phys. Rev. Lett.* **88**, 067901 (2002).
- [30] S. F. Yelin, K. Kirby, and R. Côté, Schemes for robust quantum computation with polar molecules, *Phys. Rev. A* **74**, 050301(R) (2006).
- [31] J. Zhu, S. Kais, Q. Wei, D. Herschbach, and B. Friedrich, Implementation of quantum logic gates using polar molecules in pendular states, *J. Chem. Phys.* **138**, 024104 (2013).
- [32] F. Herrera, Y. Cao, S. Kais, and K. B. Whaley, Infrared-dressed entanglement of cold open-shell polar molecules for universal matchgate quantum computing, *New J. Phys.* **16**, 075001 (2014).
- [33] K.-K. Ni, T. Rosenband, and D. D. Grimes, Dipolar exchange quantum logic gate with polar molecules, *Chem. Sci.* **9**, 6830 (2018).
- [34] R. Sawant, J. A. Blackmore, P. D. Gregory, J. Mur-Petit, D. Jaksch, J. Aldegunde, J. M. Hutson, M. R. Tarbutt, and S. L. Cornish, Ultracold molecules as qudits, *New J. Phys.* **22**, 013027 (2020).
- [35] M. Hughes, M. D. Frye, R. Sawant, G. Bhole, J. A. Jones, S. L. Cornish, M. R. Tarbutt, J. M. Hutson, D. Jaksch, and J. Mur-Petit, Robust entangling gate for polar molecules using magnetic and microwave fields, *Phys. Rev. A* **101**, 062308 (2020).
- [36] K.-K. Ni, S. Ospelkaus, M. H. G. de Miranda, A. Pe'er, B. Neyenhuis, J. J. Zirbel, S. Kotochigova, P. S. Julienne, D. S. Jin, and J. Ye, A high phase-space-density gas of polar molecules, *Science* **322**, 231 (2008).
- [37] J. G. Danzl, E. Haller, M. Gustavsson, M. J. Mark, R. Hart, N. Bouloufa, O. Dulieu, H. Ritsch, and H.-C. Nägerl, Quantum gas of deeply bound ground state molecules, *Science* **321**, 1062 (2008).
- [38] F. Lang, K. Winkler, C. Strauss, R. Grimm, and J. Hecker Denschlag, Ultracold Triplet Molecules in the Rovibrational Ground State, *Phys. Rev. Lett.* **101**, 133005 (2008).
- [39] T. Takekoshi, L. Reichsöllner, A. Schindewolf, J. M. Hutson, C. R. Le Sueur, O. Dulieu, F. Ferlaino, R. Grimm, and H.-C. Nägerl, Ultracold Dense Samples of Dipolar RbCs Molecules in the Rovibrational and Hyperfine Ground State, *Phys. Rev. Lett.* **113**, 205301 (2014).
- [40] P. K. Molony, P. D. Gregory, Z. Ji, B. Lu, M. P. Köpinger, C. R. Le Sueur, C. L. Blackley, J. M. Hutson, and S. L. Cornish, Creation of Ultracold $^{87}\text{Rb}^{133}\text{Cs}$ Molecules in the Rovibrational Ground State, *Phys. Rev. Lett.* **113**, 255301 (2014).
- [41] J. W. Park, S. A. Will, and M. W. Zwierlein, Ultracold Dipolar Gas of Fermionic $^{23}\text{Na}^{40}\text{K}$ Molecules in Their Absolute Ground State, *Phys. Rev. Lett.* **114**, 205302 (2015).
- [42] F. Seeßelberg, N. Buchheim, Z.-K. Lu, T. Schneider, X.-Y. Luo, E. Tiemann, I. Bloch, and C. Gohle, Modeling the adiabatic creation of ultracold polar $^{23}\text{Na}^{40}\text{K}$ molecules, *Phys. Rev. A* **97**, 013405 (2018).
- [43] H. Yang, D.-C. Zhang, L. Liu, Y.-X. Liu, J. Nan, B. Zhao, and J.-W. Pan, Observation of magnetically tunable feshbach resonances in ultracold $^{23}\text{Na}^{40}\text{K} + ^{40}\text{K}$ collisions, *Science* **363**, 261 (2019).
- [44] M. Guo, B. Zhu, B. Lu, X. Ye, F. Wang, R. Vexiau, N. Bouloufa-Maafa, G. Quémener, O. Dulieu, and D. Wang, Creation of an Ultracold Gas of Ground-State Dipolar $^{23}\text{Na}^{87}\text{Rb}$ Molecules, *Phys. Rev. Lett.* **116**, 205303 (2016).
- [45] T. M. Rvachov, H. Son, A. T. Sommer, S. Ebadi, J. J. Park, M. W. Zwierlein, W. Ketterle, and A. O. Jamison, Long-Lived Ultracold Molecules with Electric and Magnetic Dipole Moments, *Phys. Rev. Lett.* **119**, 143001 (2017).
- [46] H. Hara, Y. Takasu, Y. Yamaoka, J. M. Doyle, and Y. Takahashi, Quantum Degenerate Mixtures of Alkali and Alkaline-Earth-Like Atoms, *Phys. Rev. Lett.* **106**, 205304 (2011).
- [47] R. Roy, R. Shrestha, A. Green, S. Gupta, M. Li, S. Kotochigova, A. Petrov, and C. H. Yuen, Photoassociative production of ultracold heteronuclear YbLi^* molecules, *Phys. Rev. A* **94**, 033413 (2016).
- [48] A. Guttridge, M. D. Frye, B. C. Yang, J. M. Hutson, and S. L. Cornish, Two-photon photoassociation spectroscopy of CsYb:

- Ground-state interaction potential and interspecies scattering lengths, *Phys. Rev. A* **98**, 022707 (2018).
- [49] V. Barbé, A. Ciamei, B. Pasquiou, L. Reichsöllner, F. Schreck, P. S. Żuchowski, and J. M. Hutson, Observation of Feshbach resonances between alkali and closed-shell atoms, *Nat. Phys.* **14**, 881 (2018).
- [50] M. D. Frye, S. L. Cornish, and J. M. Hutson, Prospects of Forming High-Spin Polar Molecules from Ultracold Atoms, *Phys. Rev. X* **10**, 041005 (2020).
- [51] A. Green, J. H. SeeToh, R. Roy, M. Li, S. Kotochigova, and S. Gupta, Two-photon photoassociation spectroscopy of the $^2\Sigma^+$ YbLi molecular ground state, *Phys. Rev. A* **99**, 063416 (2019).
- [52] E. S. Shuman, J. F. Barry, and D. DeMille, Laser cooling of a diatomic molecule, *Nature (London)* **467**, 820 (2010).
- [53] J. F. Barry, D. J. McCarron, E. B. Norrgard, M. H. Steinecker, and D. DeMille, Magneto-optical trapping of a diatomic molecule, *Nature (London)* **512**, 286 (2014).
- [54] D. J. McCarron, E. B. Norrgard, M. H. Steinecker, and D. DeMille, Improved magneto-optical trapping of a diatomic molecule, *New J. Phys.* **17**, 035014 (2015).
- [55] E. B. Norrgard, D. J. McCarron, M. H. Steinecker, M. R. Tarbutt, and D. DeMille, Submillikelvin Dipolar Molecules in a Radio-Frequency Magneto-Optical Trap, *Phys. Rev. Lett.* **116**, 063004 (2016).
- [56] M. T. Hummon, M. Yeo, B. K. Stuhl, A. L. Collopy, Y. Xia, and J. Ye, 2D Magneto-Optical Trapping of Diatomic Molecules, *Phys. Rev. Lett.* **110**, 143001 (2013).
- [57] V. Zhelyazkova, A. Cournol, T. E. Wall, A. Matsushima, J. J. Hudson, E. A. Hinds, M. R. Tarbutt, and B. E. Sauer, Laser cooling and slowing of CaF molecules, *Phys. Rev. A* **89**, 053416 (2014).
- [58] S. Truppe, H. J. Williams, M. Hambach, L. Caldwell, N. J. Fitch, E. A. Hinds, B. E. Sauer, and M. R. Tarbutt, Molecules cooled below the Doppler limit, *Nat. Phys.* **13**, 1173 (2017).
- [59] L. Anderegg, B. L. Augenbraun, Y. Bao, S. Burchesky, L. W. Cheuk, W. Ketterle, and J. M. Doyle, Laser cooling of optically trapped molecules, *Nat. Phys.* **14**, 890 (2018).
- [60] J. Lim, J. R. Almond, M. A. Trigatzis, J. A. Devlin, N. J. Fitch, B. E. Sauer, M. R. Tarbutt, and E. A. Hinds, Laser Cooled YbF Molecules for Measuring the Electron's Electric Dipole Moment, *Phys. Rev. Lett.* **120**, 123201 (2018).
- [61] I. Kozyryev, L. Baum, K. Matsuda, B. L. Augenbraun, L. Anderegg, A. P. Sedlack, and J. M. Doyle, Sisyphus Laser Cooling of a Polyatomic Molecule, *Phys. Rev. Lett.* **118**, 173201 (2017).
- [62] L. R. Hunter, S. K. Peck, A. S. Greenspon, S. S. Alam, and D. DeMille, Prospects for laser cooling TIF, *Phys. Rev. A* **85**, 012511 (2012).
- [63] T. Chen, W. Bu, and B. Yan, Radiative deflection of a BaF molecular beam via optical cycling, *Phys. Rev. A* **96**, 053401 (2017).
- [64] G. Z. Iwata, R. L. McNally, and T. Zelevinsky, High-resolution optical spectroscopy with a buffer-gas-cooled beam of BaH molecules, *Phys. Rev. A* **96**, 022509 (2017).
- [65] P. Aggarwal, V. R. Marshall, H. L. Bethlem, A. Boeschoten, A. Borschevsky, M. Denis, K. Esajas, Y. Hao, S. Hoekstra, K. Jungmann, T. B. Meijnecht, M. C. Mooij, R. G. E. Timmermans, A. Touwen, W. Ubachs, S. M. Vermeulen, L. Willmann, Y. Yin, and A. Zapara (NL-eEDM Collaboration), Lifetime measurements of the $A^2\Pi_{1/2}$ and $A^2\Pi_{3/2}$ states in BaF, *Phys. Rev. A* **100**, 052503 (2019).
- [66] A. Micheli, G. Pupillo, H. P. Büchler, and P. Zoller, Cold polar molecules in two-dimensional traps: Tailoring interactions with external fields for novel quantum phases, *Phys. Rev. A* **76**, 043604 (2007).
- [67] L. Pollet, J. D. Picon, H. P. Büchler, and M. Troyer, Supersolid Phase with Cold Polar Molecules on a Triangular Lattice, *Phys. Rev. Lett.* **104**, 125302 (2010).
- [68] B. Capogrosso-Sansone, C. Trefzger, M. Lewenstein, P. Zoller, and G. Pupillo, Quantum Phases of Cold Polar Molecules in 2D Optical Lattices, *Phys. Rev. Lett.* **104**, 125301 (2010).
- [69] W. Lechner and P. Zoller, From Classical to Quantum Glasses with Ultracold Polar Molecules, *Phys. Rev. Lett.* **111**, 185306 (2013).
- [70] A. V. Gorshkov, S. R. Manmana, G. Chen, J. Ye, E. Demler, M. D. Lukin, and A. M. Rey, Tunable Superfluidity and Quantum Magnetism with Ultracold Polar Molecules, *Phys. Rev. Lett.* **107**, 115301 (2011).
- [71] A. V. Gorshkov, S. R. Manmana, G. Chen, E. Demler, M. D. Lukin, and A. M. Rey, Quantum magnetism with polar alkali-metal dimers, *Phys. Rev. A* **84**, 033619 (2011).
- [72] Y. L. Zhou, M. Ortner, and P. Rabl, Long-range and frustrated spin-spin interactions in crystals of cold polar molecules, *Phys. Rev. A* **84**, 052332 (2011).
- [73] K. R. A. Hazzard, S. R. Manmana, M. Foss-Feig, and A. M. Rey, Far-from-Equilibrium Quantum Magnetism with Ultracold Polar Molecules, *Phys. Rev. Lett.* **110**, 075301 (2013).
- [74] M. Greiner, O. Mandel, T. Esslinger, T. W. Hänsch, and I. Bloch, Quantum phase transition from a superfluid to a mott insulator in a gas of ultracold atoms, *Nature (London)* **415**, 39 (2002).
- [75] S. A. Moses, J. P. Covey, M. T. Miecnikowski, B. Yan, B. Gadway, J. Ye, and D. S. Jin, Creation of a low-entropy quantum gas of polar molecules in an optical lattice, *Science* **350**, 659 (2015).
- [76] L. Reichsöllner, A. Schindewolf, T. Takekoshi, R. Grimm, and H.-C. Nägerl, Quantum Engineering of a Low-Entropy Gas of Heteronuclear Bosonic Molecules in an Optical Lattice, *Phys. Rev. Lett.* **118**, 073201 (2017).
- [77] J. G. Danzl, M. J. Mark, E. Haller, M. Gustavsson, R. Hart, J. Aldegunde, J. M. Hutson, and H.-C. Nägerl, An ultracold high-density sample of rovibronic ground-state molecules in an optical lattice, *Nat. Phys.* **6**, 265 (2010).
- [78] R. Vexiau, D. Borsalino, M. Lepers, A. Orbán, M. Aymar, O. Dulieu, and N. Bouloufa-Maafa, Dynamic dipole polarizabilities of heteronuclear alkali dimers: Optical response, trapping and control of ultracold molecules, *Int. Rev. Phys. Chem.* **36**, 709 (2017).
- [79] J. Aldegunde, B. A. Rivington, P. S. Żuchowski, and J. M. Hutson, Hyperfine energy levels of alkali-metal dimers: Ground-state polar molecules in electric and magnetic fields, *Phys. Rev. A* **78**, 033434 (2008).
- [80] J. Aldegunde, H. Ran, and J. M. Hutson, Manipulating ultracold polar molecules with microwave radiation: The influence of hyperfine structure, *Phys. Rev. A* **80**, 043410 (2009).

- [81] H. Ran, J. Aldegunde, and J. M. Hutson, Hyperfine structure in the microwave spectra of ultracold polar molecules, *New J. Phys.* **12**, 043015 (2010).
- [82] J. M. Brown and A. Carrington, *Rotational Spectroscopy of Diatomic Molecules* (Cambridge University Press, Cambridge, 2003).
- [83] G. Herzberg, *Spectra of Diatomic Molecules*, Molecular Spectra and Molecular Structure, Vol. 1 (van Nostrand, Princeton, NJ, 1950).
- [84] J. Aldegunde and J. M. Hutson, Hyperfine structure of alkali-metal diatomic molecules, *Phys. Rev. A* **96**, 042506 (2017).
- [85] P. D. Gregory, J. A. Blackmore, J. Aldegunde, J. M. Hutson, and S. L. Cornish, ac stark effect in ultracold polar $^{87}\text{Rb}^{133}\text{Cs}$ molecules, *Phys. Rev. A* **96**, 021402(R) (2017).
- [86] P. D. Gregory, J. Aldegunde, J. M. Hutson, and S. L. Cornish, Controlling the rotational and hyperfine state of ultracold $^{87}\text{Rb}^{133}\text{Cs}$ molecules, *Phys. Rev. A* **94**, 041403(R) (2016).
- [87] S. A. Will, J. W. Park, Z. Z. Yan, H. Loh, and M. W. Zwierlein, Coherent Microwave Control of Ultracold $^{23}\text{Na}^{40}\text{K}$ Molecules, *Phys. Rev. Lett.* **116**, 225306 (2016).
- [88] M. Guo, X. Ye, J. He, G. Quémener, and D. Wang, High-resolution internal state control of ultracold $^{23}\text{Na}^{87}\text{Rb}$ molecules, *Phys. Rev. A* **97**, 020501(R) (2018).
- [89] Q. Wei, S. Kais, B. Friedrich, and D. Herschbach, Entanglement of polar molecules in pendular states, *J. Chem. Phys.* **134**, 124107 (2011).
- [90] M. Li, A. Petrov, C. Makrides, E. Tiesinga, and S. Kotochigova, Pendular trapping conditions for ultracold polar molecules enforced by external electric fields, *Phys. Rev. A* **95**, 063422 (2017).
- [91] S. Kotochigova and D. DeMille, Electric-field-dependent dynamic polarizability and state-insensitive conditions for optical trapping of diatomic polar molecules, *Phys. Rev. A* **82**, 063421 (2010).
- [92] B. Neyenhuis, B. Yan, S. A. Moses, J. P. Covey, A. Chotia, A. Petrov, S. Kotochigova, J. Ye, and D. S. Jin, Anisotropic Polarizability of Ultracold Polar $^{40}\text{K}^{87}\text{Rb}$ Molecules, *Phys. Rev. Lett.* **109**, 230403 (2012).
- [93] F. Seeßelberg, X.-Y. Luo, M. Li, R. Bause, S. Kotochigova, I. Bloch, and C. Gohle, Extending Rotational Coherence of Interacting Polar Molecules in a Spin-Decoupled Magic Trap, *Phys. Rev. Lett.* **121**, 253401 (2018).
- [94] J. A. Blackmore, L. Caldwell, P. D. Gregory, E. M. Bridge, R. Sawant, J. Aldegunde, J. Mur-Petit, D. Jaksch, J. M. Hutson, B. E. Sauer, M. R. Tarbutt, and S. L. Cornish, Ultracold molecules for quantum simulation: Rotational coherences in CaF and RbCs, *Quantum Sci. Technol.* **4**, 014010 (2018).
- [95] D. J. McCarron, H. W. Cho, D. L. Jenkin, M. P. Köppinger, and S. L. Cornish, Dual-species Bose-Einstein condensate of ^{87}Rb and ^{133}Cs , *Phys. Rev. A* **84**, 011603(R) (2011).
- [96] M. P. Köppinger, D. J. McCarron, D. L. Jenkin, P. K. Molony, H. W. Cho, S. L. Cornish, C. R. Le Sueur, C. L. Blackley, and J. M. Hutson, Production of optically trapped $^{87}\text{RbCs}$ Feshbach molecules, *Phys. Rev. A* **89**, 033604 (2014).
- [97] P. D. Gregory, P. K. Molony, M. P. Köppinger, A. Kumar, Z. Ji, B. Lu, A. L. Marchant, and S. L. Cornish, A simple, versatile laser system for the creation of ultracold ground state molecules, *New J. Phys.* **17**, 055006 (2015).
- [98] P. K. Molony, A. Kumar, P. D. Gregory, R. Kliese, T. Puppe, C. R. Le Sueur, J. Aldegunde, J. M. Hutson, and S. L. Cornish, Measurement of the binding energy of ultracold $^{87}\text{Rb}^{133}\text{Cs}$ molecules using an offset-free optical frequency comb, *Phys. Rev. A* **94**, 022507 (2016).
- [99] P. K. Molony, P. D. Gregory, A. Kumar, C. R. Le Sueur, J. M. Hutson, and S. L. Cornish, Production of ultracold $^{87}\text{Rb}^{133}\text{Cs}$ in the absolute ground state: Complete characterisation of the STIRAP transfer, *ChemPhysChem.* **17**, 3811 (2016).
- [100] A. R. Allouche, M. Korek, K. Fakherddin, A. Chaalan, M. Dagher, F. Taher, and M. Aubert-Frécon, Theoretical electronic structure of RbCs revisited, *J. Phys. B* **33**, 2307 (2000).
- [101] O. Docenko, M. Tamanis, R. Ferber, T. Bergeman, S. Kotochigova, A. V. Stoliarov, A. de Faria Nogueira, and C. E. Fellows, Spectroscopic data, spin-orbit functions, and revised analysis of strong perturbative interactions for the $A^1\Sigma^+$ and $b^3\Pi$ states of RbCs, *Phys. Rev. A* **81**, 042511 (2010).
- [102] P. D. Gregory, M. D. Frye, J. A. Blackmore, E. M. Bridge, R. Sawant, J. M. Hutson, and S. L. Cornish, Sticky collisions of ultracold RbCs molecules, *Nat. Commun.* **10**, 3104 (2019).
- [103] P. D. Gregory, J. A. Blackmore, S. L. Bromley, and S. L. Cornish, Loss of Ultracold $^{87}\text{Rb}^{133}\text{Cs}$ Molecules Via Optical Excitation of Long-Lived Two-Body Collision Complexes, *Phys. Rev. Lett.* **124**, 163402 (2020).
- [104] H. Fahs, A. R. Allouche, M. Korek, and M. Aubert-Frécon, The theoretical spin-orbit structure of the RbCs molecule, *J. Phys. B* **35**, 1501 (2002).
- [105] A. Christianen, M. W. Zwierlein, G. C. Groenenboom, and T. Karman, Photoinduced Two-Body Loss of Ultracold Molecules, *Phys. Rev. Lett.* **123**, 123402 (2019).
- [106] M. S. Safronova, B. Arora, and C. W. Clark, Frequency-dependent polarizabilities of alkali-metal atoms from ultraviolet through infrared spectral regions, *Phys. Rev. A* **73**, 022505 (2006).
- [107] For the data and analysis presented in this work. See the data repository at: DOI:[10.15128/r1gh93gz505](https://doi.org/10.15128/r1gh93gz505)
- [108] The python 3.7 code for hyperfine structure calculations is available at: DOI:[10.5281/ZENODO.3755881](https://doi.org/10.5281/ZENODO.3755881)